ACS APPLIED MATERIALS & INTERFACES

Research Article

Cite This: ACS Appl. Mater. Interfaces 2018, 10, 35623−35630

www.acsami.org

Essential Role of Spinel $ZnFe_2O_4$ Surfaces during Lithiation

Haoyue Guo,[†] Amy C. Marschilok,[†,‡] Kenneth J. Takeuchi,[†,‡] Esther S. Takeuchi,[†,‡,§] and Ping Liu*[,†,∥]

[†]Department of Chemistry and [‡]Department of Materials Science and Chemical Engineering, Stony Brook University, Stony Brook, New York 11794, United States

[§]Energy Sciences Directorate and [∥]Chemistry Department, Brookhaven National Laboratory, Upton, New York 11793, United States

Supporting Information

ABSTRACT: Spinel zinc ferrite ($ZnFe_2O_4$) is a well-known anode material in lithium ion batteries (LIBs) because of its large theoretical capacity. However, the high potentials observed at the initial stage of lithiation cannot be captured using a model of Li^+ intercalation into the stoichiometric $ZnFe_2O_4$ bulk. Here, using density functional theory, we report for the first time that the $ZnFe_2O_4$ surfaces are responsible for the measured initial potentials. Among the three identified stable surfaces, $ZnFeO_2$-terminated $ZnFe_2O_4$(1 1 0), O-terminated $ZnFe_2O_4$(1 1 1), and Zn-terminated $ZnFe_2O_4$(1 1 1), both (1 1 1) surfaces display higher lithiation potentials than the (1 1 0) surface, and the estimated potentials based on Zn-terminated (1 1 1) fit well with the experimental observations, whereas using the models based on $ZnFe_2O_4$(1 1 0) and previously $ZnFe_2O_4$ bulk, the estimated potentials are much lower. In terms of Li^+ diffusion, the Zn-terminated $ZnFe_2O_4$(1 1 1) surface is the most active, where the energetically favorable saturation of Li^+ on the surface is able to facilitate the process. Our results provide a new strategy for the design of LIB materials, via controlling the particle shape and the associated surface characteristics, thus enhancing the discharging performance.

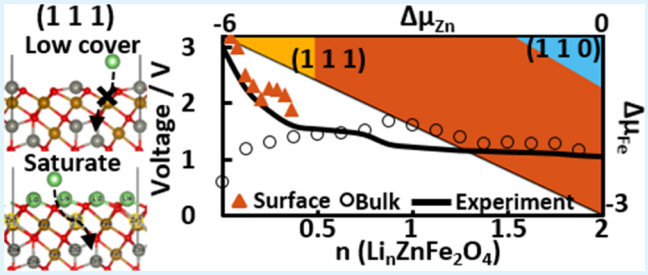

KEYWORDS: *$ZnFe_2O_4$, DFT, surface stability, Li absorption, Li diffusion, Li-ion batteries*

INTRODUCTION

Zinc ferrite ($ZnFe_2O_4$) is a prospective anode material for lithium ion batteries (LIBs) owing to its large theoretical capacity (1000 mA h/g), good structural stability, facile preparation method, and low toxicity.[1,2] Although the structure of $ZnFe_2O_4$ bulk has been well studied, the origin of the high performance of $ZnFe_2O_4$ as LIB materials is not well understood, in particular the detailed fundamental understanding of the lithiation mechanism, which is essential to optimize the performance of $ZnFe_2O_4$.

Previously, we have employed density functional theory (DFT) to successfully describe the mechanism at the initial stage lithiation of $ZnFe_2O_4$ up to $Li_nZnFe_2O_4$ ($n \leq 2$) using bulk models.[1,3] Our calculations identified the key lithiation intermediates and were able to describe well the experimentally measured open-circuit voltages (OCVs) for $n \geq 0.5$. However, the model failed to describe the initial lithiation stage with $n < 0.5$, where the predicted OCVs were lower than the corresponding measured values.[1,3] Such phenomena are not specific for $ZnFe_2O_4$ and have also been reported for other LIBs materials, for example, Fe_3O_4.[4] Our hypothesis is that the discrepancy is associated with the surfaces of $ZnFe_2O_4$, where the initial lithiation likely occurs. On the surfaces, the interaction with Li^+ can be enhanced via the presence of either the active ions with lower coordination than those in bulk or the defect sites formed upon interacting with the chemical environments. Moreover, the detailed understanding of the surface will be very helpful to provide guidelines for future LIB material design, such as coating, doping, or controlled fabrication of $ZnFe_2O_4$ to improve its electrochemical performance.

Herein, we employed DFT to determine the surface structures of spinel $ZnFe_2O_4$ and describe the corresponding performance during the lithiation process. In contrast to the studies on bulk, little has been reported for the surface structures and properties of $Li_nZnFe_2O_4$. One of the focuses of previous studies was the surface structure and stability of unlithiated $ZnFe_2O_4$. According to the measurement using high-resolution transmission electron microscopy (TEM), bulk-terminated (2 2 0),[2,5,6] (1 1 1),[5−9] and (3 1 1)[2,5,8,10] were exposed facets of the crystal, and the particle morphology was sensitive to synthesis conditions. During the lithiation process, the (1 1 1) facet was found not only to be stable but also to accelerate the Li intercalation.[6] Thus, the fabrication of $ZnFe_2O_4$ with increased area of (1 1 1) facet helps in promoting the cyclability and enhancing the lithiation rate.

Received: July 29, 2018
Accepted: September 19, 2018
Published: September 19, 2018

DOI: 10.1021/acsami.8b12869
ACS Appl. Mater. Interfaces 2018, 10, 35623−35630

However, the origin of the facet-preference and the facet-dependent performance remains unknown because of the difficulty in using existing experimental tools to characterize the atomic surface structure of such a complex system.

To provide the mechanistic understanding at the atomic level, theoretical calculations were performed for $ZnFe_2O_4$. So far, to our best knowledge, there has been only one DFT study focusing on the facet-preference among the low-index (0 0 1), (1 0 0), (1 1 0), and (1 0 1) surfaces.[11] The results showed that the Zn- and Fe-terminated (1 1 0) and (1 0 1) surfaces are more stable than the Zn-terminated (0 0 1) and (1 0 0) surfaces; however, the promising (1 1 1) surface identified experimentally[1,6] was not studied. In addition, to make it energetically comparable from one surface to the next, the surface was described by a slab with different terminations on two ends, which can be very different in surface energy in some cases.[12−14] This can result in inaccuracy of the calculated facet-preference.[15]

In the present DFT study, both the low-index surfaces, (1 0 0), (1 1 0), and (1 1 1), and high-index surface of $ZnFe_2O_4$, (3 1 1), were taken into consideration, according to the previous X-ray diffraction (XRD) and TEM studies.[1,2,5−10] To eliminate the effect introduced by different terminations on both ends of a slab surface, the same terminations were chosen. In addition, according to the previous studies on similar systems, the surface energy of different terminations was defined as a function of Zn and Fe chemical potentials for comparison among different orientations.[16−19] Indeed, on the basis of the most stable surface structures, the estimated OCV values at $n < 0.5$ are able to well describe the experimental measurement, which could not be achieved previously using the bulk model.[1,3] Our results highlight the essential contribution of $ZnFe_2O_4$(1 1 1) at the initial stage of lithiation, via stabilizing Li^+ and facilitating the diffusion into bulk.

METHODS

DFT Calculations. DFT implemented in the Vienna ab initio Simulation Package[20,21] was employed. The spin-polarized DFT + U calculations were carried out with the projector augmented wave potential[22] using the Perdew−Burke−Ernzerhof exchange−correlation functional[23] and a kinetic energy cutoff of 520 eV. A Hubbard U correction of U_{eff} = 5.3 eV was applied to the Fe d orbitals. This setup was successfully used to predict the lithiation properties observed experimentally for bulk $ZnFe_2O_4$ according to our previous studies.[1,3] The Gaussian smearing method was used with the total energies converged better than 10^{-4} eV, and the final force on each atom is less than 0.02 eV $Å^{-1}$. The first Brillouin zone was sampled on a 3 × 3 × 1 k-mesh.

Surface Stability Calculations. The slab model was considered to describe various $ZnFe_2O_4$ surfaces. The surface was modeled using a 2 × 2 surface slab. The number of layers included varied depending on the termination, making sure that the slab was terminated by the same surface termination (Figure S1). A 20 Å thick vacuum was added along the direction perpendicular to the surface to avoid the artificial interactions between the slabs. During geometry optimization, the top three layers were allowed to relax with adsorbed Li^+, whereas the rest were fixed at the bulk positions.

Following the previous studies,[16−19] the stability of the surface was determined by the surface energy defined as

$$\zeta = \frac{E_{Slab} - x\mu_{Zn} - y\mu_{Fe} - z\mu_O}{2S}$$

where E_{Slab} is the total energy of $Zn_xFe_yO_z$ surfaces. μ_{Zn}, μ_{Fe}, and μ_O are the chemical potentials of Zn, Fe, and O, respectively, in the $Zn_xFe_yO_z$ surfaces; S is the surface area of the slab.

μ_{Zn}, μ_{Fe}, and μ_O have a range in which $ZnFe_2O_4$ bulk is stable

$$E_{ZnFe_2O_4} = \mu_{Zn} + 2\mu_{Fe} + 4\mu_O$$

$$\Delta\mu_{Zn} = \mu_{Zn} - E_{Zn} < 0$$

$$\Delta\mu_{Fe} = \mu_{Fe} - E_{Fe} < 0$$

$$\Delta\mu_O = \mu_O - E_O < 0$$

where E_{Zn}, E_{Fe}, and E_O are the total energy of metallic Zn bulk, metallic Fe bulk, and O in gaseous molecular O_2, respectively, and $\Delta\mu_{Zn}$, $\Delta\mu_{Fe}$, and $\Delta\mu_O$ refer to the difference of chemical potential in the slab and in metallic bulk (Zn and Fe) or gas phase (O), at 0 K and 1 bar. Therefore, a more negative value indicates a Zn- or Fe-poor condition, whereas a value close to 0 represents a Zn- or Fe-rich environment condition. This method has been proven previously, being able to describe well the experimental results of metal compound surfaces including $LiMn_2O_4$.[16−19]

Therefore, the surface energy was expressed as a function of $\Delta\mu_{Zn}$ and $\Delta\mu_{Fe}$

$$\zeta = \vartheta - \frac{(x - z/4)\Delta\mu_{Zn} + (y - z/2)\Delta\mu_{Fe}}{2S}$$

where ϑ is a constant and measures the surface stability with respect to $ZnFe_2O_4$ bulk and metallic Zn and Fe. On the basis of the equations, the phase diagrams of various surfaces with different terminations of $ZnFe_2O_4$ were determined.

Lithiation Reactivity Calculations. The Li absorption/binding energy is defined as[24]

$$E_b = E_{nLi/Surface} - E_{Surface} - nE_{Li^+}$$

where $E_{nLi/Surface}$, $E_{Surface}$, and E_{Li^+} correspond to the total energy of the Li-adsorbed surface, bare surface, and aqueous Li^+ ion, respectively. n is the number of Li on the surface. Negative E_b represents an energetically favorable adsorption.

The average intercalation voltage is calculated by[25]

$$V = \frac{E_{nLi/Surface} - E_{Surface} - nE_{Li}}{nF}$$

where E_{Li} stands for the total energy of Li bulk and F is the Faraday's constant.

RESULTS AND DISCUSSION

$ZnFe_2O_4$ Surfaces: Structures and Stability. $ZnFe_2O_4$ adopts a normal spinel structure, in which the equivalent positions are divided into six different groups, 8a, 8b, 16c, 16d, 32e, and 48f sites. The octahedral 16d sites are occupied by Fe^{3+}, whereas Zn^{2+} and O^{2-} take up the tetrahedral 8a sites and octahedral 32e sites, respectively. The vacancy sites, including octahedral 16c and tetrahedral 48f and 8b, are available for Li insertion and/or diffusion. Our calculations started with the previously optimized bulk $ZnFe_2O_4$ structure in the $Fd\bar{3}m$ primitive cell and containing eight formula units.[1,3] The DFT-optimized lattice parameters of 8.54 Å (8.45 Å in experiment[1]) and magnetic moments of 4.3 μB (4.2 μB in experiment[26]) are in good agreement with the values measured experimentally. The surface stabilities of low-index surfaces, (1 0 0), (1 1 0), and (1 1 1), and the high-index surface (3 1 1) with various bulk terminations of $ZnFe_2O_4$ were considered. The phase diagrams based on the calculated ζ were plotted to reveal the most stable structures as a function of $\Delta\mu_{Zn}$ and $\Delta\mu_{Fe}$.

Various terminations of $ZnFe_2O_4$(1 0 0), $ZnFe_2O_4$(1 1 0), $ZnFe_2O_4$(1 1 1), and $ZnFe_2O_4$(3 1 1) surfaces were considered (Figures S2−S5), where each termination was expressed by the corresponding composition in our notation. On the basis of the calculated ζ, Figure 1 summarizes the most stable surface

DOI: 10.1021/acsami.8b12869
ACS Appl. Mater. Interfaces 2018, 10, 35623−35630

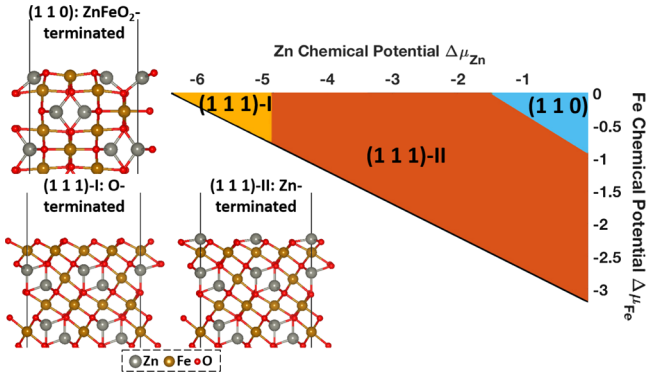

Figure 1. Phase diagram and the corresponding structures of stable terminations of $ZnFe_2O_4$(1 1 0) and (1 1 1) surfaces.

structures as a function of $\Delta\mu_{Zn}$ and $\Delta\mu_{Fe}$. Among the four surfaces studied for $ZnFe_2O_4$, the (1 1 1) and (1 1 0) surfaces were found to be stable under a range of chemical potentials for which $ZnFe_2O_4$ bulk is stable. Specifically, in both the Zn-rich and Fe-rich regions, the stoichiometric $ZnFeO_2$-terminated $ZnFe_2O_4$(1 1 0) is stable. In the Zn-poor and Fe-rich regions, the O-terminated $ZnFe_2O_4$(1 1 1) surface, (1 1 1)-I in our notation, is preferred. The Zn-terminated $ZnFe_2O_4$(1 1 1) surface, (1 1 1)-II in our notation, is the most likely surface configuration, which covers the relatively large area in the phase diagram including Zn-rich and Fe-poor as well as extensive intermediate regions. Our results indicate that (1 1 1) is likely the dominant facet in spinel $ZnFe_2O_4$, which agrees well with the previous experiments using XRD, TEM, and calculations on spinel LIB materials.[5−9,18]

According to the DFT calculations, both $ZnFe_2O_4$(1 0 0) and $ZnFe_2O_4$(3 1 1) are not stable under the range of chemical potentials for which $ZnFe_2O_4$ bulk is stable (Figure 1). The (3 1 1) surface observed in XRD and TEM for $ZnFe_2O_4$ may be associated with the corresponding particle size in the nanoscale, where the stepped surfaces, such as (3 1 1), are more preferred to accommodate the curvature than the extended surfaces, such as (1 1 1). However, the structure on the terrace of (3 1 1) adopts that on (1 1 1) (Figure S5).

The (1 1 1)-I surface is constructed by a FeO_6 octahedron layer, which is parallel to the surface (Figure S1b,c). With the increasing Zn amount in the environment, the (1 1 1) surface goes from (1 1 1)-I terminated by oxygen from the FeO_6 octahedron layer (Figures 1 and S1b) to (1 1 1)-II by stacking Zn^{2+} ions over the FeO_6 octahedrons (Figures 1 and S1c). (1 1 1) is the only surface orientation of $ZnFe_2O_4$ in our study, being able to maintain the stable FeO_6 octahedron layer on the surface.

According to the projected density of states (PDOS) (Figure 2a,b), the presence of the FeO_6 octahedron layer is the key for the high stability and preference for the (1 1 1) surface. Similar distributions of Zn 3d orbitals were observed for Zn positioned on the surface and in the sublayer of $ZnFe_2O_4$(1 1 1). The results show a strong overlap with O 2p orbitals mainly around −5 eV and therefore the existence of Zn in a divalent ionic state (Figure 2b,c). This is a result of the low electronegativity of Zn, which easily loses two electrons to form stable Zn^{2+} in interaction with an oxidizing agent, such as oxygen in this case. Accordingly, the presence of Zn on the surface depends on the availability of a Zn resource, whereas the corresponding effect on the surface stability is relatively small. Thus, at the Zn-poor region, (1 1 1)-I is preferred, and with the increasing Zn amount, (1 1 1)-II becomes favorable (Figure 1). However, this is not the case for Fe. As shown in Figure 2a, the top of the valance bands, 0−5 eV, is mainly composed of O 2s, 2p. There are some contributions from Fe 3d states, which associate with partially reduced Fe^{2+} because of the formation of surfaces. Our calculations show that the amount of reduced Fe^{2+} exposed on the surface is a descriptor to determine the surface stability. The more reduced Fe ions result in the higher the surface energy. It is only when the surface Fe ions are present in the form of a FeO_6 octahedron layer, as in the case of (1 1 1)-I, II (Figure 1), that the contribution from the reduced Fe^{2+}

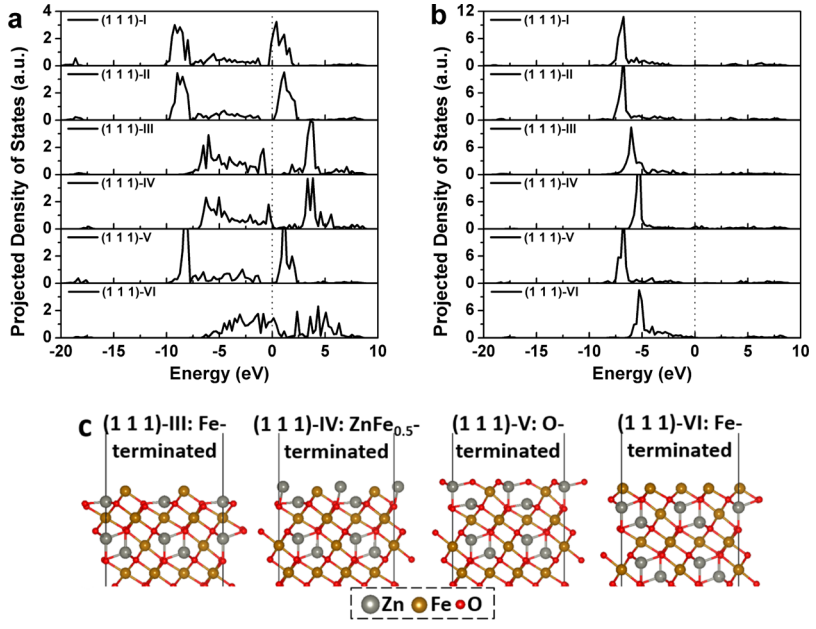

Figure 2. PDOS of surface Fe^{3+} (a) and Zn^{2+} (b) on $ZnFe_2O_4$(1 1 1) with different terminations, going from $ZnFe_2O_4$(1 1 1)-I to $ZnFe_2O_4$(1 1 1)-VI surfaces, where the corresponding structures of $ZnFe_2O_4$(1 1 1)-III−VI are shown in (c).

DOI: 10.1021/acsami.8b12869
ACS Appl. Mater. Interfaces 2018, 10, 35623−35630

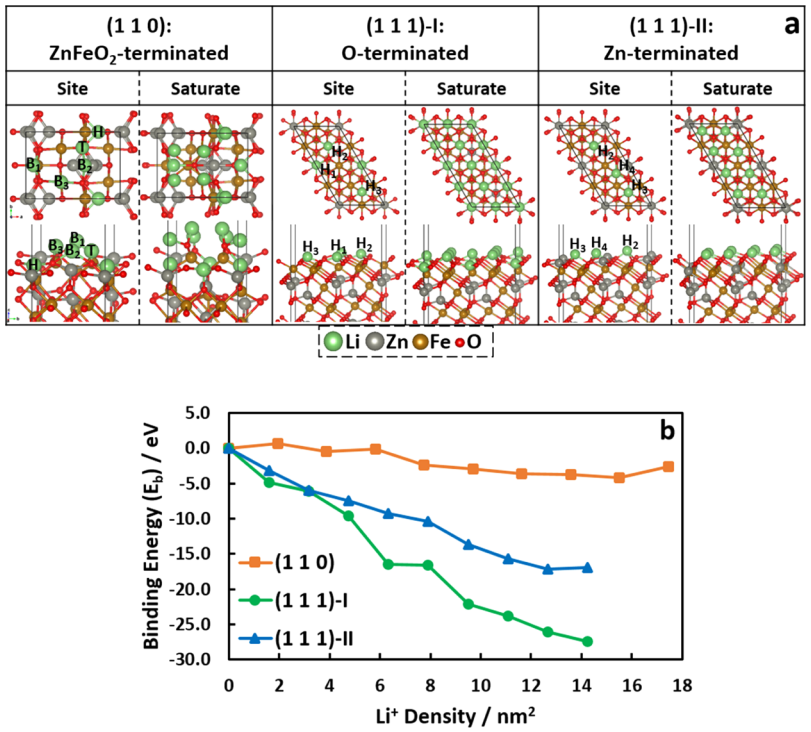

Figure 3. (a) Li^+ adsorption sites on bare $ZnFe_2O_4$(1 1 0), (1 1 1)-I, and (1 1 1)-II surfaces and the corresponding structures under Li^+ saturation. (b) Variation in binding energy (E_b) with the density of Li^+ on the surface.

is small; by comparison, more Fe^{2+} states are observed for the (1 1 1) surfaces with other terminations, (1 1 1)-III, IV, V, V, where the FeO_6 octahedron layers are broken on the formation of the surface (Figure 2c). As a result, the corresponding surface becomes less stable than (1 1 1)-I, II, where the FeO_6 octahedron layer remains intact.

The identification of stable $ZnFe_2O_4$ surfaces allows us to estimate the effect of surfaces on the lithiation performance during the initial stage of lithiation. The contribution from surfaces is associated with the corresponding capability in capturing Li^+ and providing a feasible path for Li^+ to transport into the bulk. Accordingly, Li^+ adsorption on the surface and diffusion from the surface to the sublayer were studied on the following stable surfaces, $ZnFe_2O_4$(1 1 0), $ZnFe_2O_4$(1 1 1)-I, and $ZnFe_2O_4$(1 1 1)-II (Figure 1).

Li^+ Absorption and Average Voltage. *$ZnFe_2O_4$(1 1 0).* On (1 1 0), various top (T), bridge (B), and hollow (H) sites were considered for Li^+ adsorption, where the adsorptions at three sites, O−O-bridge (B_1−O, B_2−O, and B_3−O in our notation), survived after geometry optimization (Figure 3a). However, all of them are not energetically favorable (E_b = 0.63 eV at B_1−O, E_b = 1.66 eV at B_2−O, and E_b = 0.88 eV at B_3−O) (Figure 3b). The difference between B_1−O and B_2−O sites is that the presence of surface Zn^{2+} between the two O^{2-} of the B_2−O site provides a strong repulsion and makes the Li^+ absorption energetically less favorable than that on the B_1−O site. A similar situation is observed for the B_3−O site, yet the repulsive interaction is less intensive with Fe^{3+} positioned underneath further away from the surface. The O-top (T−O in our notation) and O−O−O-hollow (H−O in our notation) sites are not stable for initial Li^+ adsorption and Li^+ shifts to the B_1−O site after optimization.

With the increasing coverage of Li^+, the preferential adsorption position varies from the B_1−O site to the T−O site (Figure S6), which is accompanied with increasing surface distortion. This enhances the corresponding E_b going from positive to negative values (Figure 3b). In addition, the saturation of the (1 1 0) surface by Li^+ is energetically favorable up to 15.51 Li/nm^2 with an energy gain of 4.23 eV and all T−O sites occupied (Figures 3a and S6). After saturation, the adsorption of an additional Li^+ ion is hindered, which costs 1.60 eV. This is due to the strong repulsion from the previously adsorbed Li^+ ions together with strong structural distortions (Figure S6). Overall, the ability of the (1 1 0) surface to capture the Li^+ ion during the lithiation process is rather low. Moreover, the structural distortion is significant under high Li^+ coverage, indicating that the (1 1 0) surface is not stable during the Li^+ absorption process and may lead to low cyclability.

$ZnFe_2O_4$(1 1 1)-I. On (1 1 1)-I, three sites were identified as being able to stabilize the Li^+ ion, including the O−O−O-fcc hollow site (H_1−O in our notation, E_b = −4.81 eV; H_3−O in our notation, E_b = −2.72 eV) and O−O−O-hcp hollow site (H_2−O in our notation, E_b = −3.34 eV) (Figure 3a). At low coverage of Li^+, the H_1−O site is the most active for adsorption, whereas the presence of a Fe^{3+} ion underneath of H_2−O hinders the adsorption of Li^+ via electrostatic repulsion. The least active is the H_3−O site. The three O−O sides that construct the H_3−O sites are involved in the formation of three stable FeO_6 octahedral units. The strong Fe−O interactions make them too rigid to allow the same structural flexibility as is the case of H_1−O and thus achieve strong binding. Nevertheless, all of the H−O sites on (1 1 1) are able to provide much stronger binding than that on (1 1 0) because of its larger cavity and higher coordination with O. This preference of Li^+ adsorption on (1 1 1) over (1 1 0) increases with the increasing coverage of Li^+ (Figures 3b and S6), even though the additional adsorbed Li^+ ions have to occupy the

DOI: 10.1021/acsami.8b12869
ACS Appl. Mater. Interfaces 2018, 10, 35623−35630

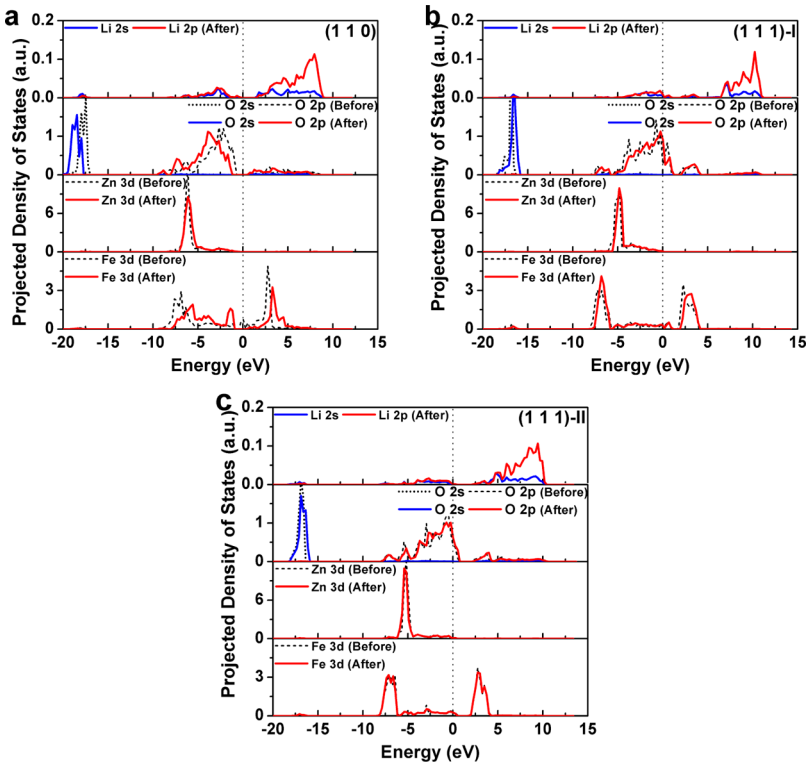

Figure 4. PDOS of surface ions before and after adsorption of Li^+ at the low coverage on $ZnFe_2O_4$(1 1 0) (a), $ZnFe_2O_4$(1 1 1)-I (b), and $ZnFe_2O_4$(1 1 1)-II (c).

less stable H_2−O site. The energy release from Li^+ adsorption on (1 1 1)-I increases from 4.81 eV at low coverage (surface density: 1.58 Li/nm^2) to 26.04 eV at the saturated coverage (12.66 Li/nm^2) where the two active sites, $H_{1,2}$−O, are both occupied. The further increase in Li^+ coverage to 14.25 Li/nm^2 forces the previously adsorbed Li^+ ion to diffuse to the octahedral 16c site in the 1st sublayer, with an energy cost of 1.37 eV.

$ZnFe_2O_4$(1 1 1)-II. On (1 1 1)-II, because the most preferred H_1−O sites as the case of (1 1 1)-I are occupied by Zn^{2+}, the Li^+ ion prefers to adsorb at the O−O−O-fcc hollow site (H_4−O in our notation). This is different from that on (1 1 1)-I, where the adsorption on H_4−O is not stable and spontaneously shifts to the H_1−O site. Yet, the corresponding binding (E_b = −3.19 eV) is not as strong as that on the H_1−O site on (1 1 1)-I. In this case, the three O−O sides surrounding the H_4−O site are part of either a FeO_6 octahedral or a ZnO_3 unit (Figure 3a), which promotes the stability of O^{2-} ions and hinders the stabilization of Li^+. This is also the case for the adsorption at the H_2−O (E_b = −2.18 eV) sites and H_3−O (E_b = −1.67 eV), where the presence of Zn^{2+} on the surface promotes the rigidity of the H−O sites and deactivates the sites for Li^+ adsorption as compared to that on (1 1 1)-I. The binding of Li^+ on (1 1 1)-II increases with an increasing Li^+ coverage, where the adsorption site varies from the most active H_4−O site to the H_3−O site (Figures 3b and S6). Even though Li^+ is initially adsorbed on the H_2−O site, it displaces to H_3−O sites after geometry optimization. It can be attributed to the fact that the H_2 site is neighboring to the adsorbed Li^+ ions at high coverage of 9.50 Li/nm^2 and becomes destabilized because of the strong lateral repulsion. Upon going to the saturated coverage of 12.66 Li/nm^2, the corresponding energy gain (−17.21 eV) is less than that of (1 1 1)-I (Figure 3b). During this process, the Zn^{2+} ions on the surface are very mobile, displacing from the surface to the octahedral 16c sites in the 1st sublayer and blocking the typical 16c → 16c pathway for Li^+ diffusion from the surface to the bulk (Figure 3a). The further addition of Li^+ at the coverage of 14.25 Li/nm^2 is not energetically favorable with an energy cost of 0.29 eV because of the lateral repulsion from the neighboring absorbed Li^+ ions (Figures 3b and S6).

Three stable surfaces of $ZnFe_2O_4$ are likely to be saturated by Li^+ ions up to 15.51 Li/nm^2 according to the thermodynamics. During the lithiation process, Li is the electron donor. With the formation of Li−O coordinate bonds over the $ZnFe_2O_4$ surfaces, about 1 electron is transferred from a Li atom to the system, which is demonstrated by the limited states right below the Fermi level according to the calculated PDOS (Figure 4). Fe 3d states are delocalized significantly, whereas the variation in Zn^{2+} is relatively small. This indicates that the surface Fe^{3+} sites are partially reduced and are the electron acceptors during the lithiation process.

The capability to capture Li^+ is different. Both (1 1 1) surfaces are able to bind Li^+ more strongly than the (1 1 0) surface ranging from the low Li coverage to the saturated coverage (Figure 3b). This is also confirmed by the PDOS (Figure 4), where less occupied states are observed for the adsorbed Li^+ on $ZnFe_2O_4$(1 1 1)-I,II surfaces and therefore more stable than those on $ZnFe_2O_4$(1 1 0). The unique FeO_6 octahedron-based surface structure of (1 1 1) not only promotes the surface stability but also provides highly active H−O sites, capable of Li^+ ion capture.

To evaluate the contribution of Li^+ adsorption on the surfaces to the lithiation of $ZnFe_2O_4$, the DFT-calculated binding energies (Figure 3b) on the stable surfaces were used to estimate the average cell voltages. Here, the coverage of Li^+

DOI: 10.1021/acsami.8b12869
ACS Appl. Mater. Interfaces 2018, 10, 35623−35630

was converted to the n value in $Li_nZnFe_2O_4$. For comparison with the experimental measurements on $ZnFe_2O_4$ nanoparticles,[1] the corresponding surface areas for particles with the sizes observed experimentally were estimated. Accordingly, the number of Li^+ adsorbed and therefore the number of electron transfers were calculated and converted to n by dividing the number of $ZnFe_2O_4$ units included in the particle. In addition, the adsorption on (1 1 1)-II was chosen, which showed the higher possibility under the interested environments than (1 1 1)-I and (1 1 0) (Figure 1). The results indicate that indeed our hypothesis is right. At $n < 0.5$ (Figure 5), the estimated voltages based on the DFT-calculated

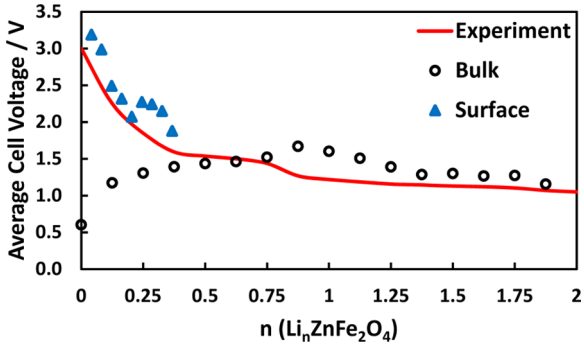

Figure 5. DFT-estimated average cell voltages on surface and bulk structures, in comparison with experimental operating voltage circuit. The bulk data points are cited from Guo, et al.,[3] and the experimental results are cited from Zhang, et al.[1]

binding energies on (1 1 1)-II align well with the experimental measurements, which cannot be achieved previously using the bulk model.[3] Such an observation confirms the importance of surface considerations during the initial lithiation stage.

Li^+ Diffusion from Surface toward Bulk. Besides the capture of Li^+, ion diffusion is also a key to the lithiation performance. To gain better understanding, we investigated the Li^+ ion diffusion from the surface toward the bulk on three stable surfaces, $ZnFe_2O_4$(1 1 0), $ZnFe_2O_4$(1 1 1)-I, and $ZnFe_2O_4$(1 1 1)-II. Three sublayers, 1st, 2nd, and 3rd sublayers (Figure S1), were defined, making a path for Li^+ transported from the surface toward the bulk. Finally, both low and saturated coverage of Li^+ ions were considered to account for the coverage effect (Figures 6, S7 and S8), as the saturation of Li^+ on three surfaces is energetically favorable (Figure 3b).

$ZnFe_2O_4$(1 1 0). At low coverage, the initial diffusion of the adsorbed Li^+ ion from the surface to the octahedral 16c site at the 1st sublayer is unfavorable with an energy loss of about 1.16 eV (Figures 6 and S7). By comparison, the further diffusion into the most stable 16c position at the 2nd and 3rd sublayers becomes more exothermic, with energy gains of about 0.70 and 2.34 eV, respectively. The Li^+ diffusion is also accompanied with the decrease in E_b from 0.63 eV on the surface to −1.25 eV in the 3rd sublayer. Given that at low coverage, the Li^+ diffusion on (1 1 0) is thermodynamically favorable overall with the energy release of 1.88 eV. However, kinetically, the barrier of at least 1.16 eV must be overcome to allow the most endothermic diffusion of Li^+ from the surface to the 1st sublayer to occur.

Our calculations show that the saturation of (1 1 0) by Li^+ is more energetically favorable than the Li^+ diffusion (Figures 3b and 6). That is, Li^+ prefers to accumulate on the surface at the initial lithiation stage to a saturated coverage before diffusion

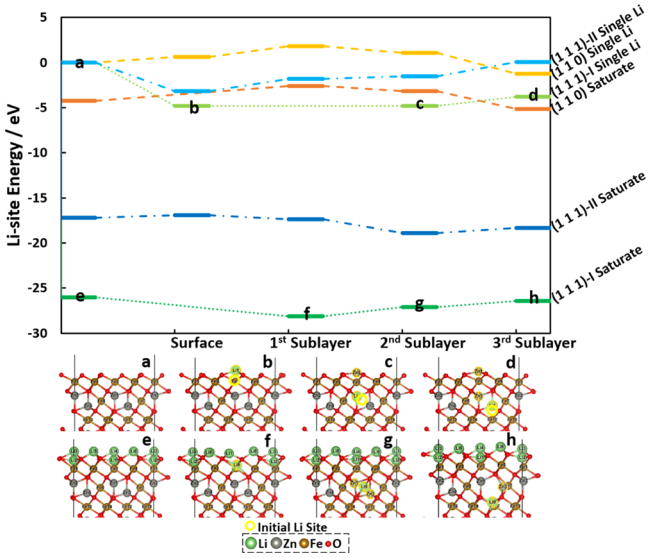

Figure 6. Top: Potential energy of Li^+ diffusion from $ZnFe_2O_4$(1 1 0), (1 1 1)-I, and (1 1 1)-II surfaces toward the bulk under low Li coverage and saturate Li coverage conditions, where the energy was expressed with respect to bare surface and aqueous Li^+ ion; bottom: The corresponding structures. (a) Bare $ZnFe_2O_4$(1 1 1)-I; (b) Li^+ adsorption on (1 1 1)-I at low coverage; (c) Li^+ diffusion to the 2nd sublayer at low coverage; (d) Li^+ diffusion to the 3rd sublayer at low coverage; (e) $ZnFe_2O_4$(1 1 1)-I saturated by Li^+; (f) Li^+ diffusion to the 1st sublayer at saturate coverage; (g) Li^+ diffusion to the 2nd sublayer at saturate coverage; and (h) Li^+ diffusion to the 3rd sublayer at saturate coverage.

toward bulk. Accordingly, the Li^+ adsorption and diffusion on the Li^+-saturated (1 1 0) surface was also studied. First, the adsorption of Li^+ is hindered and the corresponding binding is not as strong as that on the bare surface with an energy cost of 1.60 eV (Figure 3b); however, it helps the diffusion toward the bulk (Figure 6). On Li^+ adsorption, 22% of adsorbed Li^+ migrates from the surface to the octahedral 16c vacancies at the 1st sublayer (Figure S7), whereas in the case of low coverage, the further Li^+ diffusion to the 16c position at the 2nd and 3rd sublayers is more thermodynamically favorable, with the energy release of 0.56 and 1.94 eV, respectively. Again, a significant structural distortion was observed during the diffusion process, indicating the low stability of the surface (1 1 0) during the Li^+ diffusion process.

$ZnFe_2O_4$(1 1 1)-I. Li^+ adsorption on (1 1 1)-I is the most preferred among the three stable surfaces (E_b = −4.81 eV, Figure 3b). The surface site is too stable for Li^+ at low coverage to allow the diffusion to the 16c position of the 1st sublayer, which shifts back to the surface site after geometry optimization (Figure 6b). The Li^+ ions at the 16c position at the 2nd and the 3rd sublayers drive the Zn^{2+} displacement from the 8a site on the same sublayer toward the surface or upper sublayer, and the left 8a vacancy is filled by the displacement of Li^+ from the 16c site (Figure 6c,d). During this process, the diffusion from the 2nd sublayer to the 3rd sublayer is the only endothermic step with an energy cost of 0.99 eV.

On the Li^+-saturated surface, which is preferred over the diffusion into bulk, the Li^+ ions occupy all of the active surface sites (Figure 6e). Further adsorption results in spontaneous diffusion of a Li^+ ion nearby from the surface to the octahedral 16c vacancy in the 1st sublayer (Figure 6f). In this case,

DOI: 10.1021/acsami.8b12869
ACS Appl. Mater. Interfaces 2018, 10, 35623−35630

because of the high coverage of Li^+ on the surface, the diffused Li^+ ions at the 1st sublayer are stable with an energy gain of 2.10 eV. For the same reason, the displacement of Zn^{2+} toward the surface is also hindered. As a result, the diffused Li^+ to the 16c site at the 2nd and the 3rd sublayers (Figure 6g,h) can also stay; however, the corresponding process is not thermodynamically preferred with the energy cost of 1.01 and 0.71 eV, respectively.

$ZnFe_2O_4$(1 1 1)-II. At low Li^+ coverage, Li^+ is strongly adsorbed (E_b = −3.19 eV), which hinders the diffusion into the bulk, as the case of (1 1 1)-I (Figure 3b). However, differently, the pathway for the Zn^{2+} displacement from the 8a site in the sublayers toward the surface is blocked, as the H_1−O sites in (1 1 1)-II are occupied by Zn^{2+}. Instead, the neighboring Zn^{2+} ions are only distorted from the lattice 8a position when Li^+ presents at the 16c sites on the same sublayer (Figure S8). Although the Li^+ diffused to the 16c site in the sublayers remains, the corresponding process is energetically not favorable, which has energy penalties of 1.35, 0.32, and 1.55 eV for diffusion from the surface to the 1st, 2nd, and 3rd sublayers, respectively (Figures 6 and S8).

The preferential Li^+-saturation on the surface enhances the Li^+ diffusion toward bulk. On the saturated surface, the Li^+ adsorption on the H_2−O site is not favored due to the lateral repulsion from the neighboring absorbed Li^+ ions (E_b = 0.29 eV). Because the surface octahedral 16c sites are occupied by displaced Zn^{2+} ions, the diffusion of Li^+ ion to the 1st sublayer and then the 2nd sublayer can be stabilized at the 8a site, with energy gains of 0.46 and 1.67 eV, respectively (Figures 6 and S8). By comparison, the 16c site in the 3rd sublayer is less preferred and the diffusion from the 2nd sublayer costs energy of 0.55 eV. In comparison with (1 1 1)-I at saturated coverage, the Li^+ diffusion from the 1st sublayer to the 2nd and the 3rd sublayers on (1 1 1)-II is more preferential (Figure 6). This can be attributed to the fully occupied and closely packed octahedral sites in the 1st sublayer due to surface saturation, which strengthens the lattice stability (Figure S8). Indeed, a relatively small structural distortion during the Li^+ diffusion is observed for the saturated (1 1 1)-II surface.

Generally, under the lithiation conditions, all three surfaces are likely saturated by Li^+ first, followed by the Li^+ diffusion from the surface toward the bulk. In most of the cases, the 16c site is preferred in the sublayers, whereas the 8a site becomes more favorable when Zn^{2+} is mobile and a segregation path toward the surface becomes feasible. Under the surface saturation conditions, (1 1 1)-I/II surfaces are more feasible for both capture and penetration of Li^+ than (1 1 0), in addition to the higher lattice stability. Wherein, (1 1 1)-I shows higher capability in Li^+ adsorption than (1 1 1)-II, whereas the Li^+ diffusion from the surface toward the bulk is more slightly facile on (1 1 1)-II.

CONCLUSIONS

We employed DFT to study the contribution from the diverse facets of $ZnFe_2O_4$ particles during the initial stage of lithiation, which could not be described previously using the model of Li^+ intercalation into stoichiometric $ZnFe_2O_4$ bulk. Both the low-index, $ZnFe_2O_4$(1 0 0), $ZnFe_2O_4$(1 1 0), $ZnFe_2O_4$(1 1 1), and high-index, $ZnFe_2O_4$(3 1 1), surfaces were taken into consideration. The (1 1 1) surfaces terminated by either O or Zn and the (1 1 0) surface terminated by $ZnFeO_2$ were identified as stable surfaces under a range of chemical potentials for which bulk $ZnFe_2O_4$ is stable. The surface stability depends on maintaining the stable FeO_6 layer on the surface.

In terms of Li^+ capture, both (1 1 1) surfaces are more active than the (1 1 0) surface among the three identified stable facets of $ZnFe_2O_4$ particle, favoring the saturation of Li^+ on the surface (12.66 Li/nm^2). The high lithiation potentials estimated based on the Zn-terminated (1 1 1) surface fit well with the experimental observations at the initial stage, whereas the estimated potentials based on $ZnFe_2O_4$(1 1 0) and previously $ZnFe_2O_4$ bulk are much lower. The excessive amount of O^{2-} sites on the surface promotes the attraction of Li^+ from the solution to the surface and the formation of stable Li−O ionic interaction.

The Li^+ prefers to accumulate on the surface to saturated coverage before diffusion toward bulk. The adsorption of Li^+ on the saturated surface facilitates the diffusion of existing adsorbed Li toward bulk because of the electrostatic repulsion. Among the stable surfaces, both (1 1 1) surfaces not only display higher capability to allow the penetration of Li^+ than (1 1 0) but also higher lattice stability during the diffusion process. Wherein, the Li^+ diffusion from the Zn-terminated (1 1 1)-II surface toward bulk is the most feasible.

Overall, the O-terminated (1 1 1) surface displays high activity to capture Li^+ from the solution, whereas the Zn-terminated (1 1 1) surface likely promotes the diffusion of Li from the surface toward the bulk. Our results may provide a design strategy for more stable particle morphologies with enhanced lithiation reactivity.

ASSOCIATED CONTENT

Supporting Information

The Supporting Information is available free of charge on the ACS Publications website at DOI: 10.1021/acsami.8b12869.

Side views of supercells; various optimized structures; additional phase diagrams; and Li^+ diffusion behavior on surfaces (PDF)

AUTHOR INFORMATION

Corresponding Author

*E-mail: pingliu3@bnl.gov.

ORCID

Haoyue Guo: 0000-0003-3477-9203
Amy C. Marschilok: 0000-0001-9174-0474
Kenneth J. Takeuchi: 0000-0001-8129-444X
Esther S. Takeuchi: 0000-0001-8518-1047
Ping Liu: 0000-0001-8363-070X

Notes

The authors declare no competing financial interest.

ACKNOWLEDGMENTS

This work was carried out at Brookhaven National Laboratory (BNL), and was funded as part of the Center for Mesoscale Transport Properties (m2M), an Energy Frontier Research Center supported by the U.S. Department of Energy, Office of Science, Basic Energy Sciences, under award no. DE-SC0012673. MRCAT operations are supported by the Department of Energy and the MRCAT member institutions. The DFT calculations were performed using computational resources at the Center for Functional Nanomaterials at Brookhaven National Laboratory, an Office of Science User Facility, and the Scientific Data and Computing Center, a

DOI: 10.1021/acsami.8b12869
ACS Appl. Mater. Interfaces 2018, 10, 35623−35630

component of the Computational Science Initiative, at Brookhaven National Laboratory under contract no. DE-SC0012704.

REFERENCES

(1) Zhang, Y.; Pelliccione, C. J.; Brady, A. B.; Guo, H.; Smith, P. F.; Liu, P.; Marschilok, A. C.; Takeuchi, K. J.; Takeuchi, E. S. Probing the Li Insertion Mechanism of $ZnFe_2O_4$ in Li-Ion Batteries: A Combined X-Ray Diffraction, Extended X-Ray Absorption Fine Structure, and Density Functional Theory Study. *Chem. Mater.* **2017**, *29*, 4282−4292.

(2) Sharma, Y.; Sharma, N.; Rao, G. V. S.; Chowdari, B. V. R. Li-storage and Cyclability of Urea Combustion Derived ZnFe2O4 as Anode for Li-ion Batteries. *Electrochim. Acta* **2008**, *53*, 2380−2385.

(3) Guo, H.; Zhang, Y.; Marschilok, A. C.; Takeuchi, K. J.; Takeuchi, E. S.; Liu, P. A First Principles Study of Spinel $ZnFe_2O_4$ for Electrode Materials in Lithium-ion Batteries. *Phys. Chem. Chem. Phys.* **2017**, *19*, 26322−26329.

(4) Lininger, C. N.; Brady, N. W.; West, A. C. Equilibria and Rate Phenomena from Atomistic to Mesoscale: Simulation Studies of Magnetite. *Acc. Chem. Res.* **2018**, *51*, 583−590.

(5) Peng, L.; Fang, Z.; Li, J.; Wang, L.; Bruck, A. M.; Zhu, Y.; Zhang, Y.; Takeuchi, K. J.; Marschilok, A. C.; Stach, E. A.; Takeuchi, E. S.; Yu, G. Two-Dimensional Holey Nanoarchitectures Created by Confined Self-Assembly of Nanoparticles via Block Copolymers: From Synthesis to Energy Storage Property. *ACS Nano* **2018**, *12*, 820−828.

(6) Zhong, X.-B.; Jin, B.; Yang, Z.-Z.; Wang, C.; Wang, H.-Y. Facile Shape Design and Fabrication of $ZnFe_2O_4$ as an Anode Material for Li-ion Batteries. *RSC Adv.* **2014**, *4*, 55173−55178.

(7) Bresser, D.; Paillard, E.; Kloepsch, R.; Krueger, S.; Fiedler, M.; Schmitz, R.; Baither, D.; Winter, M.; Passerini, S. Carbon Coated $ZnFe_2O_4$ Nanoparticles for Advanced Lithium-Ion Anodes. *Adv. Energy Mater.* **2013**, *3*, 513−523.

(8) Rai, A. K.; Kim, S.; Gim, J.; Alfaruqi, M. H.; Mathew, V.; Kim, J. Electrochemical Lithium Storage of a $ZnFe_2O_4$/graphene Nanocomposite as an Anode Material for Rechargeable Lithium Ion Batteries. *RSC Adv.* **2014**, *4*, 47087−47095.

(9) Song, H.; Zhu, L.; Li, Y.; Lou, Z.; Xiao, M.; Ye, Z. Preparation of $ZnFe_2O_4$ Nanostructures and Highly Efficient Visible-light-driven Hydrogen Generation with the Assistance of Nanoheterostructures. *J. Mater. Chem. A* **2015**, *3*, 8353−8360.

(10) Lv, H.; Ma, L.; Zeng, P.; Ke, D.; Peng, T. Synthesis of Floriated $ZnFe_2O_4$ with Porous Nanorod Structures and its Photocatalytic Hydrogen Production Under Visible Light. *J. Mater. Chem.* **2010**, *20*, 3665−3672.

(11) Zou, C.-y.; Ji, W.; Shen, Z.; Tang, Q.; Fan, M. NH3 Molecule Adsorption on Spinel-type $ZnFe_2O_4$ Surface: A DFT and Experimental Comparison Study. *Appl. Surf. Sci.* **2018**, *442*, 778−786.

(12) Bottin, F.; Finocchi, F.; Noguera, C. Stability and Electronic Structure of the (1×1) SrTiO3 (110) Polar Surfaces by First-principles Calculations. *Phys. Rev. B: Condens. Matter Mater. Phys.* **2003**, *68*, 035418.

(13) Conesa, J. Computer Modeling of Surfaces and Defects on Cerium Dioxide. *Surf. Sci.* **1995**, *339*, 337−352.

(14) Nörenberg, H.; Harding, J. H. The Surface Structure of CeO_2(001) Single Crystals Studied by Elevated Temperature STM. *Surf. Sci.* **2001**, *477*, 17−24.

(15) Zhang, H. Z.; Wang, S. Q. First-principles Study of Ti_3AC_2 (A=Si, Al) (001) Surfaces. *Acta Mater.* **2007**, *55*, 4645−4655.

(16) Qian, G.-X.; Martin, R. M.; Chadi, D. J. First-principles study of the atomic reconstructions and energies of Ga- and As-stabilized GaAs(100) surfaces. *Phys. Rev. B: Condens. Matter Mater. Phys.* **1988**, *38*, 7649−7663.

(17) Kim, S.; Aykol, M.; Wolverton, C. Surface Phase Diagram and Stability of (001) and (111) LiMn2O4 Spinel Oxides. *Phys. Rev. B: Condens. Matter Mater. Phys.* **2015**, *92*, 115411.

(18) Warburton, R. E.; Iddir, H.; Curtiss, L. A.; Greeley, J. Thermodynamic Stability of Low- and High-Index Spinel LiMn2O4 Surface Terminations. *ACS Appl. Mater. Interfaces* **2016**, *8*, 11108−11121.

(19) Pentcheva, R.; Wendler, F.; Meyerheim, H. L.; Moritz, W.; Jedrecy, N.; Scheffler, M. Jahn-Teller Stabilization of a "Polar" Metal Oxide Surface: Fe3O4(001). *Phys. Rev. Lett.* **2005**, *94*, 126101.

(20) Kresse, G.; Furthmüller, J. Efficient iterative schemes forab initiototal-energy calculations using a plane-wave basis set. *Phys. Rev. B: Condens. Matter Mater. Phys.* **1996**, *54*, 11169−11186.

(21) Kresse, G.; Furthmüller, J. Efficiency of ab-initio total energy calculations for metals and semiconductors using a plane-wave basis set. *Comput. Mater. Sci.* **1996**, *6*, 15−50.

(22) Blöchl, P. E. Projector Augmented-wave Method. *Phys. Rev. B: Condens. Matter Mater. Phys.* **1994**, *50*, 17953−17979.

(23) Perdew, J. P.; Burke, K.; Ernzerhof, M. Generalized Gradient Approximation Made Simple. *Phys. Rev. Lett.* **1996**, *77*, 3865−3868.

(24) Mole, S. J.; Zhou, X.; Liu, R. Density Functional Theory (DFT) Study of Enthalpy of Formation. 1. Consistency of DFT Energies and Atom Equivalents for Converting DFT Energies into Enthalpies of Formation. *J. Phys. Chem.* **1996**, *100*, 14665−14671.

(25) Aydinol, M. K.; Kohan, A. F.; Ceder, G.; Cho, K.; Joannopoulos, J. Ab initiostudy of lithium intercalation in metal oxides and metal dichalcogenides. *Phys. Rev. B: Condens. Matter Mater. Phys.* **1997**, *56*, 1354−1365.

(26) Schiessl, W.; Potzel, W.; Karzel, H.; Steiner, M.; Kalvius, G. M.; Martin, A.; Krause, M. K.; Halevy, I.; Gal, J.; Schäfer, W.; Will, G.; Hillberg, M.; Wäppling, R. Magnetic Properties of the ZnFe2O4 Spinel. *Phys. Rev. B: Condens. Matter Mater. Phys.* **1996**, *53*, 9143−9152.

DOI: 10.1021/acsami.8b12869
ACS Appl. Mater. Interfaces 2018, 10, 35623−35630